

# We are IntechOpen, the world's leading publisher of Open Access books Built by scientists, for scientists

6,900

Open access books available

186,000

International authors and editors

200M

Downloads

Our authors are among the

154

Countries delivered to

TOP 1%

most cited scientists

12.2%

Contributors from top 500 universities



WEB OF SCIENCE™

Selection of our books indexed in the Book Citation Index  
in Web of Science™ Core Collection (BKCI)

Interested in publishing with us?  
Contact [book.department@intechopen.com](mailto:book.department@intechopen.com)

Numbers displayed above are based on latest data collected.  
For more information visit [www.intechopen.com](http://www.intechopen.com)



# Functional Materials Synthesis and Physical Properties

*Tatsuya Senzaki, Michiaki Matsukawa, Takanori Yonai, Haruka Taniguchi, Akiyuki Matsushita, Takahiko Sasaki and Mokoto Hagiwara*

## Abstract

A citrate pyrolysis technique is a unique route to prepare reactive precursor mixtures through an ignition process of concentrated aqueous solution. This procedure enables to synthesize highly homogeneous and fine powders for functional materials. The double-chain based superconductor  $\text{Pr}_2\text{Ba}_4\text{Cu}_7\text{O}_{15-\delta}$  and double perovskite photocatalytic semiconductor  $\text{Ba}_2\text{Tb}(\text{Bi},\text{Sb})\text{O}_6$  were synthesized by using the citrate pyrolysis technique. For the present sample with a reduction treatment for 72 h, a sharp superconducting transition appeared at an onset temperature  $T_{c,\text{on}}=26$  K accompanied by a zero-resistance state at  $T_{c,\text{zero}}=22$  K. The superconducting volume fraction estimated from the magnetization measurement showed an excellent value of  $\sim 58\%$ . Both reduction treatment in a vacuum and subsequent quenching procedure are needed to realize higher superconductivity due to further oxygen defects. The polycrystalline samples for  $\text{Ba}_2\text{Tb}(\text{Bi}_{1-x},\text{Sb}_x)\text{O}_6$  ( $x = 0$  and  $0.5$ ) were formed in the monoclinic and cubic crystal structures. We conducted the gaseous 2-propanol (IPA) and methylene blue (MB) degradation experiments under a visible light irradiation, to evaluate photocatalytic activities of the powder samples. For the Sb50% substituted sample, the highest performance of MB degradation was observed. The effect of Sb-substitution on the photocatalytic degradation of MB is in direct contrast to that on the IPA decomposition under visible light irradiation. The enhanced photocatalytic properties in the citrate samples are attributed to their morphology, where fine particles are homogeneously distributed with a submicron order.

**Keywords:** citrate pyrolysis technique, double-chain based superconductor, pressure effect, double-perovskite oxide, photocatalytic semiconductor

## 1. Introduction

A citrate pyrolysis technique is similar to nitrate combustion synthesis methods [1] and a unique route to prepare reactive precursor mixtures through an ignition process of concentrated aqueous solution including stoichiometric amounts of metal ions. For 80 K-class high-  $T_c$  cuprate superconductors such as  $\text{YBa}_2\text{Cu}_3\text{O}_7$ , high-quality single-phase polycrystalline samples have been successfully prepared at ambient oxygen pressure [2, 3]. We believe that the present technique is a powerful tool to fabricate highly homogeneous and fine crystalline grains for functional materials, in comparison to conventional solid-state reaction methods.

High-  $T_c$  copper-oxide superconductors discovered as far have close relationship with two-dimensional  $\text{CuO}_2$  planes. In quasi one-dimensional (1D)  $\text{Cu}_2\text{O}_3$  ladder system without  $\text{CuO}_2$  planes, it has been reported in [4] that the application of external pressure under 3 GPa causes bulk superconductivity at  $T_c = 12$  K. For Pr-based copper oxides including insulating  $\text{CuO}_2$  planes, we have reported that  $\text{Pr}_2\text{Ba}_4\text{Cu}_7\text{O}_{15-\delta}$  (Pr247) with metallic  $\text{CuO}$  double-chain structure achieves a superconducting-state with a higher  $T_c$  (15 K) after a reduction treatment [5].

In the subsequent microscopic research on Pr247 [6], nuclear quadrupole resonance observations have resolved that the newly discovered superconductivity occurs along the  $\text{CuO}$  double-chain block. The Pr-based cuprates,  $\text{PrBa}_2\text{Cu}_3\text{O}_{7-\delta}$  (Pr123) and  $\text{PrBa}_2\text{Cu}_4\text{O}_8$  (Pr124), have identical crystal structures as Y-based high- $T_c$  superconductors,  $\text{YBa}_2\text{Cu}_3\text{O}_{7-\delta}$  (Y123) and  $\text{YBa}_2\text{Cu}_4\text{O}_8$  (Y124), respectively. Both the Pr123 and Pr124 compounds share insulating  $\text{CuO}_2$  planes and exhibit no superconductivity [7, 8]. The  $\text{CuO}$  single chains in Pr123 follow semiconducting property but Pr124 has a metallic conduction along the  $\text{CuO}$  double chain block [9]. For Pr124, it is hard to control the carrier density of doped double chains, because it is thermally stable against high temperature heat treatment.

For Pr247 intermediate compound existing between Pr123 and Pr124 phases, there are alternate stacks of  $\text{CuO}$  single-chain and double-chain blocks along the  $c$ -axis such as  $\{-S-D-S-D-\}$  sequence [10, 11] (see **Figure 1**). Here,  $\text{CuO}$  single-chain and double-chain blocks along the  $b$ -axis are abbreviated as S and D, respectively. Under thermal control of the oxygen content along the semiconducting  $\text{CuO}$  single chains in Pr247, it is possible to investigate the physical characters of the metallic  $\text{CuO}$  double chains. In oxygen defect polycrystalline sample, we succeeded in the appearance of superconductivity at an onset temperature  $T_{c,\text{on}}$  of  $\sim 15$  K [5].

The B-site substituted perovskite oxides  $\text{A}_2\text{B}'\text{B}''\text{O}_6$  have been widely studied because of their attractive physical properties and potential applications [13] (see **Figure 2a**). Some of the double perovskite compounds such as  $\text{A}_2\text{FeMoO}_6$  exhibiting negative tunneling magnetoresistance effect at room temperature are of great interest with a wide range of applications in magnetic devices [14]. Furthermore, multiferroic double perovskite oxides have an effective coupling between spontaneous ferroelectric polarization and ferromagnetic ordering, which is considered to be promising materials from view points of physics and its applications [15]. Recently, a series of double perovskite oxides  $\text{Ba}_2\text{Ln}'\text{Bi}''\text{O}_6$  (Ln:lanthanides) has been examined on the view point of photocatalytic semiconductors for hydrogen generation by water splitting and are taken as alternative materials for  $\text{TiO}_2$  oxide [16, 17]. In particular,  $\text{Ba}_2\text{PrBiO}_6$  is found to possess highly photocatalytic performance, which is probably close to the valence mixing state [18, 19]. Furthermore, a previous study on the magnetic properties of the  $\text{Ba}_2\text{PrBiO}_6$  compound revealed that the average valence of Pr ions is an intermediate state between trivalent and tetravalent [20].

As for the key factors to fabricate visible light driven photocatalysts, it is desirable to control the energy band gap between the valence and conduction bands of their semiconductors to utilize a wide range of visible light [21, 22]. Accordingly, we think that the Sb substitution at the B site of the parent material  $\text{Ba}_2\text{PrBiO}_6$  is an effective approach to adjusting the band gaps. For high photocatalytic activity, we avoid charge recombination between electron and hole and try to promote the photogenerated charge separation in the photocatalytic materials [21, 23]. In our research [24], it has been demonstrated that the valence mixing states between  $\text{Pr}^{3+}$  and  $\text{Pr}^{4+}$  are closely related to the phenomena of charge separation.

For our further understanding of the enhanced effect of the mixed valence states at B-site ions of the double perovskite compound on the photocatalytic

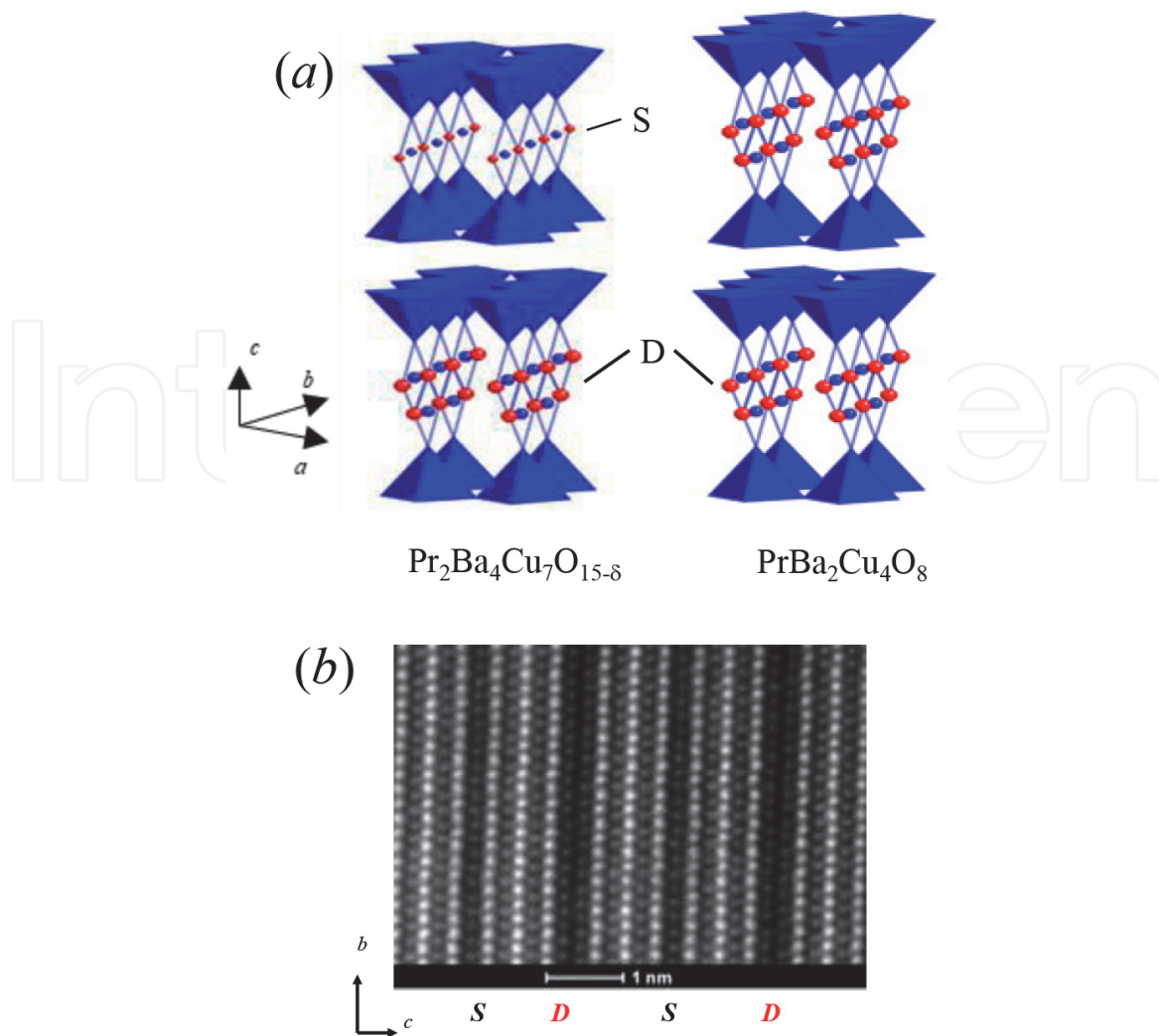


**Figure 1.**

(a) Typical crystal structure of  $\text{Pr}_2\text{Ba}_4\text{Cu}_7\text{O}_{15-\delta}$  (Pr247) with CuO single-chain and double-chain blocks stacked along the  $c$ -axis. Here, S and D denote CuO single-chain and double-chain blocks along the  $b$ -axis. For comparison, the crystal structure of Pr124 is shown on the right hand side. (b) TEM image of superconducting Pr247. CuO single-chain and double-chain blocks are alternately stacked along the  $c$ -axis such as  $\{-S-D-S-D-\}$  sequence [12].

performance, we demonstrate the 2-propanol decomposition and methylene blue (MB) degradation under the irradiation of visible light for  $\text{Ba}_2\text{Tb}(\text{Bi},\text{Sb})\text{O}_6$  samples prepared by the citrate pyrolysis technique. MB aqueous solution is adopted as the model pollutant [25].

## 2. Experiments

### 2.1 Double-chain based superconductor

#### 2.1.1 Synthesis of $\text{Pr}_2\text{Ba}_4\text{Cu}_7\text{O}_{15-\delta}$ samples

First of all, flow chart of citrate pyrolysis technique for the synthesis of  $\text{Pr}_2\text{Ba}_4\text{Cu}_7\text{O}_{15-\delta}$  (sample #1) is illustrated in **Figure 3b**. We synthesized high-quality polycrystalline samples of  $\text{Pr}_2\text{Ba}_4\text{Cu}_7\text{O}_{15-\delta}$  by using a citrate pyrolysis technique [2, 3]. Stoichiometric quantities of high purity  $\text{Pr}_6\text{O}_{11}$ ,  $\text{Ba}(\text{NO}_3)_2$ , and CuO were mixed and thoroughly ground. The mixture was dissolved in a nitric acid solution at 50–60°C. After adding citric acid to the resultant solution, we then neutralized it by adding aqueous

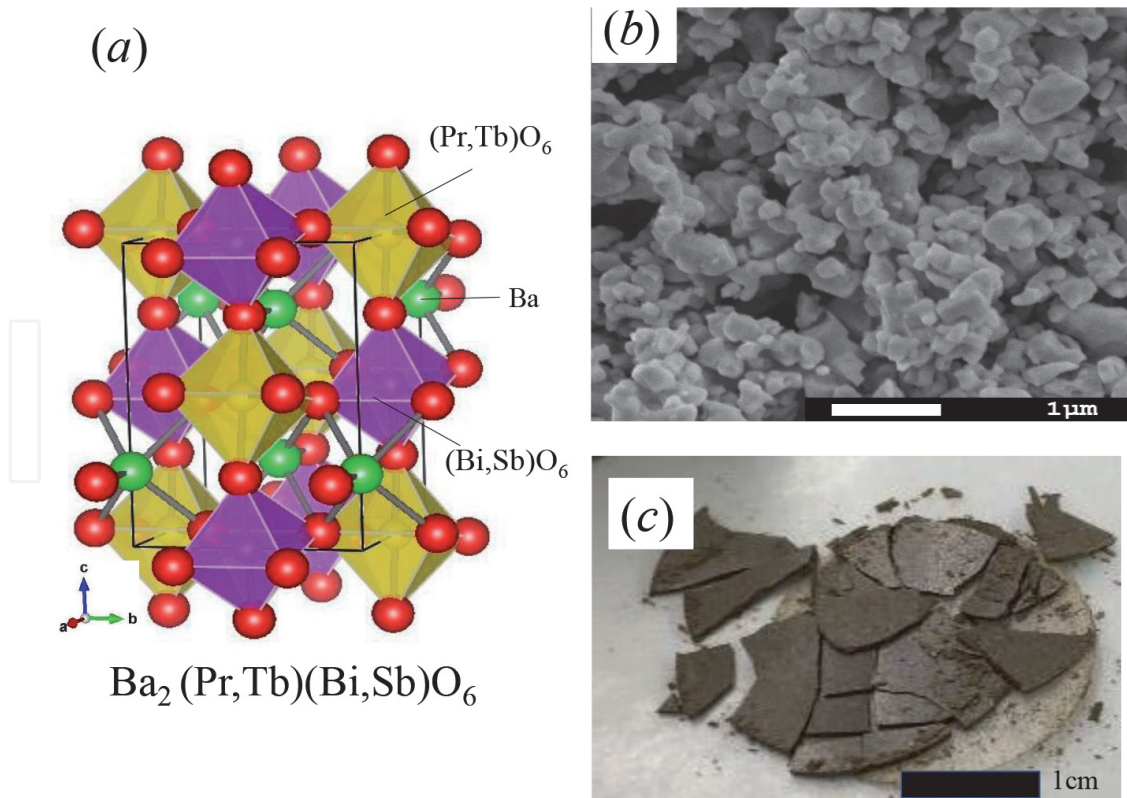


**Figure 2.**

(a) Typical crystal structure of double perovskite  $Ba_2(Pr,Tb)(Bi,Sb)O_6$ . (b) SEM image of  $Ba_2TbBiO_6$  polycrystalline film fabricated from the single-phase powders by an electrophoretic deposition technique. (c) Photograph of the pelletized precursors of  $Ba_2TbBiO_6$  after a citrate pyrolysis procedure.

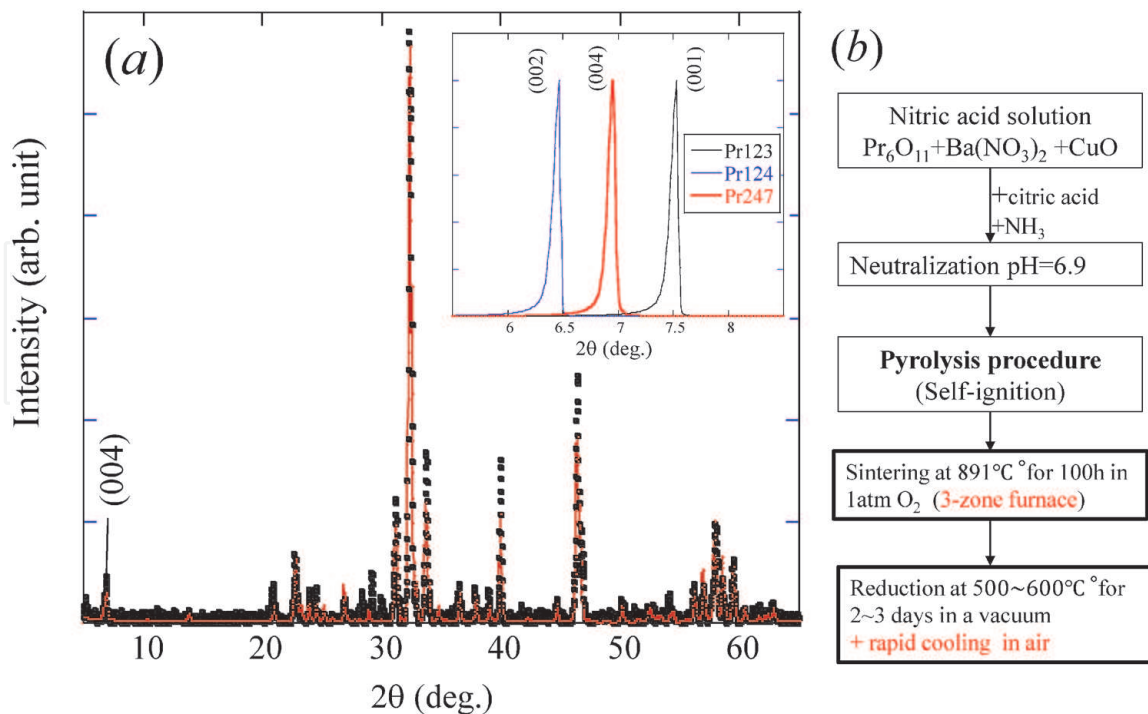


**Figure 3.**

(a) X-ray diffraction patterns of as-sintered polycrystalline  $Pr_2Ba_4Cu_7O_{15-\delta}$ . The (004) peak corresponds to one of typical Miller indexes of  $Pr_{247}$ . The calculated curve is obtained using the lattice parameters in the text. Inset shows characteristic peaks at  $2\theta \sim 7^\circ$ , indicating the formation of  $Pr_{123}$ ,  $Pr_{124}$ , and  $Pr_{247}$  phases. (b) Flow chart of citrate pyrolysis technique for the synthesis of  $Pr_2Ba_4Cu_7O_{15-\delta}$  (sample #1). After post-annealing of the as-sintered sample in a vacuum, quenching procedure is needed to obtain higher superconductivity due to further oxygen defects.

ammonia. After the solution was dried up under stirring on halogen lamp heater block, the porous black products were formed through the self-ignition process of it. Finally, the precursors were ground into fine powders and they were annealed under ambient pressure of flowing oxygen gas at  $891^{\circ}\text{C} \pm 0.5^{\circ}\text{C}$  for an extended period over 100~120 h. For the present citrate pyrolysis synthesis procedure, we adopted the electric tube furnace with three zone temperature controlled system, to achieve the temperature uniformity within  $1^{\circ}\text{C}$ . In our previous study [26], we realized homogeneous distributions of the superconducting grains and improved weak links between their superconducting grains in the sintering procedure by using the 3 zone furnace. The oxygen in the as-sintered sample was removed by reduction treatment in a vacuum at  $500\sim 600^{\circ}\text{C}$ , yielding a superconducting material. In particular, sample #1 was quenched in air from  $300^{\circ}\text{C}$  down to room temperature and samples #2-1 and #2-2 were slowly cooled in the electric furnace, as listed in **Table 1**. As mentioned below, this quenching procedure is needed to obtain higher superconductivity due to further oxygen defects. Typical dimensions of the pelletized rectangular sample were  $4 \times 3 \times 1 \text{ mm}^3$ .

### 2.1.2 Structural and physical properties of $\text{Pr}_2\text{Ba}_4\text{Cu}_7\text{O}_{15-\delta}$ samples

X-ray diffraction measurements on the produced samples were carried out at room temperature with an Ultima IV diffractometer (Rigaku) using Cu-K $\alpha$  radiation. We evaluated the lattice parameters from the x-ray diffraction patterns using the least-squares fits.

The local crystal structure of the Pr247 sample was revealed by high-resolution transmission electron microscopy (TEM) using a JEOL3010 microscope operated at 300 kV at Tohoku University, to examine alternative stacking along the *c*-axis between CuO single-chain and double-chain blocks. The electric resistivity as a function of temperature was measured by the *dc* four-terminal method using a Gifford-McMahon cryocooler (Sumitomo heavy Industries).

We performed Hall coefficient measurements on the 48-h-reduced samples with the five-probe technique using a physical property measuring system (PPMS, Quantum Design), to check the sign of carriers in the present Pr247 superconductor. For determination of an onset temperature of superconductivity and superconducting volume fraction at low temperatures, the *dc* magnetization was performed under zero-field cooling (ZFC) in a commercial superconducting quantum interference device (SQUID) magnetometer (MPMS, Quantum Design).

### 2.1.3 Pressure effect on transport properties of $\text{Pr}_2\text{Ba}_4\text{Cu}_7\text{O}_{15-\delta}$ samples

It is well known that application of external pressure on oxide superconductors changes doped carrier densities, causing a positive or negative dependence of their

Sample no.	Reduced condition	$\delta$	$T_{c,on}$ (K)	$T_{c,zero}$ (K)	Experimental data
#1	500°C 48 h, 600°C 24 h quenched	0.72	26	22	$\rho(T)$ , $M(T)$
#2-1 <sup>a</sup>	500°C 48 h furnace cooled	0.56	26.5	15	TEM
#2-2 <sup>b</sup>	500°C 48 h furnace cooled	0.56	26.5	15	$R_H$ , pressure effect

In details, see the corresponding text and references.  $\delta$  denotes oxygen deficiency.

<sup>a</sup>Ref. [12].

<sup>b</sup>Ref. [27].

**Table 1.**  
 Sample details of  $\text{Pr}_2\text{Ba}_4\text{Cu}_7\text{O}_{15-\delta}$  used in the experiments.

superconducting transition temperature. We carried out the temperature dependence of the resistivity and the magneto-resistance (MR), under a maximum pressure of 2 GPa.

The MR effect of Pr247 sample was measured at low temperatures as a function of applied field up to 14 T using a 15 T-SM superconducting magnet at Institute for Materials Research, Tohoku University. The electric current  $I$  was excited in the longitudinal direction to the sample and the external magnetic field  $H$  was applied in the transverse direction to it ( $H \perp I$ ). We measured the influence of applied pressure on the electric resistivity using a hybrid piston cylinder-type CuBe/NiCrAl cell under hydrostatic pressure up to 2.0 GPa, where inner and outer cylinders were made of NiCrAl and CuBe alloys, respectively. A mixture of Fluorinert FC-70 and FC77 (1:1) was used as a pressure transmitting medium in the experiments.

## 2.2 Double perovskite photocatalytic semiconductor

### 2.2.1 Synthesis of $Ba_2Tb(Bi,Sb)O_6$ samples

The citrate pyrolysis technique as mentioned above was applied to synthesis of  $Ba_2Tb(Bi,Sb)O_6$  compounds. After mixing stoichiometric quantities of high purity Ba  $(NO_3)_2$ ,  $Tb_4O_7$ ,  $Bi_2O_3$ , and Sb, the resultant mixture was dissolved in a nitric acid solution at 70–80°C. Furthermore, adding citric acid to the solution, the neutralizing process was in progress by adding aqueous ammonia to it while the pH value of the solution reached  $\sim 6.9$ . The transparent solution was dried under stirring on the halogen lamp hot plate, and the self-ignition process occurred in the 0.5 L beaker, resulting in the formation of the porous products. Finally, the precursors were ground into fine powders and they were annealed in air at 900–1000°C for 48–96 h, in order to synthesize the  $Ba_2Tb(Bi,Sb)O_6$  double perovskite phase (samples #T1 and #T2).

For scanning electron microscope (SEM) measurements,  $Ba_2TbBiO_6$  polycrystalline film on Ag substrate was fabricated from the single-phase powders by an electrophoretic deposition technique. The SEM image revealed the surface morphology and shape of the  $Ba_2TbBiO_6$  powder sample.

### 2.2.2 Physical properties of $Ba_2Tb(Bi,Sb)O_6$ samples

We measured optical spectra by a diffuse reflectance method using a spectrophotometer (Hitachi U-3500) with the reference material of  $BaSO_4$ . The energy band gaps for the powder samples were estimated from the reflectance data on the basis of conventional Kubelka-Munk function [18, 28]. The *dc* magnetization measurement was performed over a wide range of temperatures under the magnetic field cooling process of 0.1 T using a SQUID magnetometer.

The effective magnetic moment ( $\mu_{\text{eff}}$ ) estimated from the the magnetic susceptibility data using the Curie–Weiss law gives rise to the average valence of the Tb ion at the B site, which is related to the ratio of the  $Tb^{3+}$  and  $Tb^{4+}$  ions.

### 2.2.3 Photocatalytic properties of $Ba_2Tb(Bi,Sb)O_6$ samples

We conducted the gaseous 2-propanol (IPA) and methylene blue (MB) degradation experiments, to evaluate photocatalytic activities of the powder samples (in detail, refer to [18, 29]). The visible light radiation experiment started after the IPA gas concentration reached constant under the dark condition. This conformation suggested that the IPA gas finished absorbing on the surface of powders. We used a 300 W Xe lamp equipped with UV and IR filtering functions (Cemax LX300F,

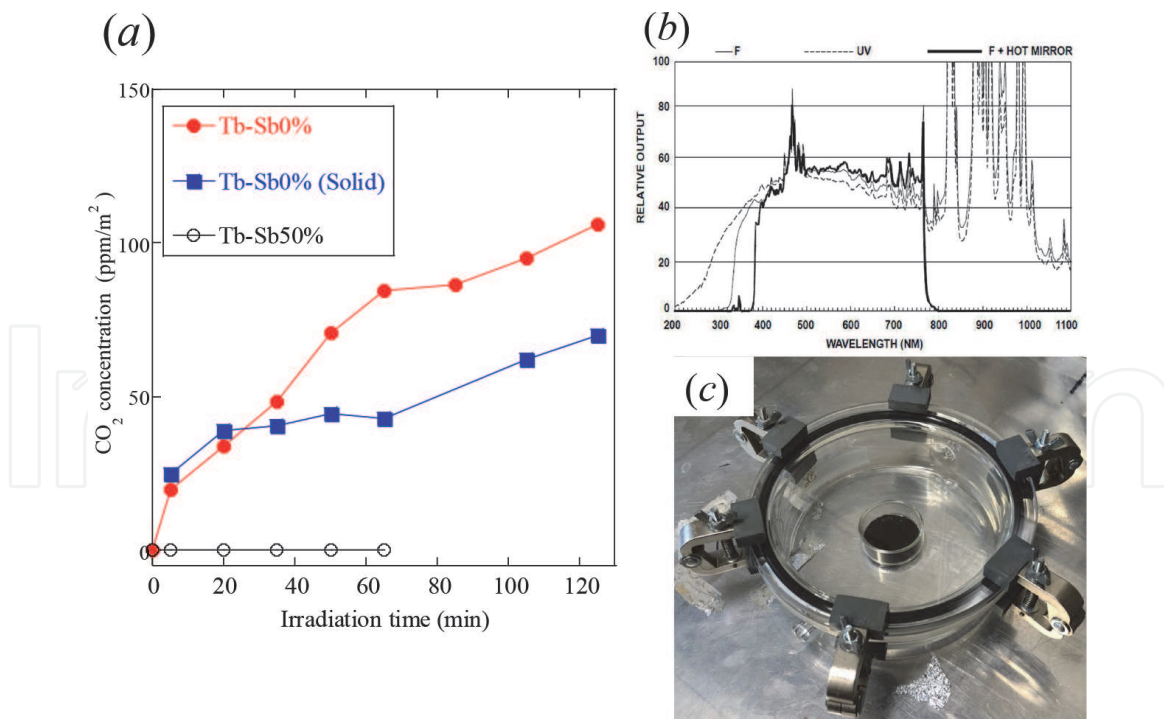


**Figure 4.** (a) Photocatalytic activities of IPA decomposition vs visible light irradiation time for Ba<sub>2</sub>TbBiO<sub>6</sub> citrate pyrolysis and solid-state samples. For comparison, the data for the Sb50% substituted sample are given. The gaseous concentration is normalized by the surface area of the powder samples. (b) Illuminating spectra of the Xe lamp limited in the visible wavelength range between 390 and 780 nm. (c) Photograph of 0.5-L glass reactor vessel for the IPA experiment. The powder sample (about 1 g) placed on the bottom of a small glass cell was set in its vessel.

Excelitas Technologies). The illuminating spectra of the Xe lamp covered the visible wavelength range from 390 to 780 nm (**Figure 4b**). We set the powder samples (about 1 g) placed on the bottom of a small glass cell in a 0.5-L glass reactor vessel (**Figure 4c**) and injected the dilute IPA gas (5 cc) into its vessel with a syringe.

It is well known that the IPA gas under photocatalytic reaction is finally decomposed into CO<sub>2</sub> [29]. Accordingly, the CO<sub>2</sub> concentration was measured as a function of irradiation time using a gas chromatography system (GC-2014, Shimazu Co.). The photocatalytic methylene blue degradation was carried out using 0.5 g of powders suspended in 50 mL of MB solution (10 ppm). The MB solution was stirred in dark for 30 min before starting visible light radiation. The bleaching of MB was measured using the UV–visible spectrometer (V550, JASCO Co.). The solution of about 3 mL was transferred from the 100 mL reactor vessel under light irradiation and it was then analyzed at the regular time interval, to determine the corresponding MB concentration.

### 3. Results and discussion

#### 3.1 Double-chain based superconductor Pr<sub>2</sub>Ba<sub>4</sub>Cu<sub>7</sub>O<sub>15-δ</sub>

##### 3.1.1 Structural and superconducting properties of Pr<sub>2</sub>Ba<sub>4</sub>Cu<sub>7</sub>O<sub>15-δ</sub>

X-ray diffraction data revealed that the as-sintered polycrystalline samples are an almost single phase with an orthorhombic structure (*Ammm*), as shown in **Figure 3a**. The lattice parameters of the as-sintered sample prepared using the three-zone controlled furnace are  $a = 3.8919 \text{ \AA}$ ,  $b = 3.9143 \text{ \AA}$ , and  $c = 50.7927 \text{ \AA}$ .

These values fairly agree with the lattice parameters of Pr247 estimated by a previous study [30]. It was from gravimetric analysis estimated that the oxygen deficiencies in the 48 and 72 h reduced samples in a vacuum are  $\delta \approx 0.56$  and  $\delta \approx 0.72$ , corresponding to samples #2-1, #2-2 and sample #1, respectively (**Table 1**). According to a variation in  $T_c$  as a function of the oxygen deficiency [31], the  $T_{c,on}$  shows a rapid increase at  $\delta \geq \sim 0.2$ , then follows a stable increase with  $\delta$ , and finally remains saturation around 26–27 K at  $\delta \geq \sim 0.6$ . Therefore, we conclude that the doped carrier concentrations in the present samples are located near the optimally doped region.

First of all, the temperature dependences of electric resistivities of the Pr123, Pr124, and as-sintered Pr247 compounds are shown in **Figure 5a**. The Pr123 and Pr124 samples exhibit semiconducting and metallic behaviors in  $\rho$ . The as-sintered Pr247 sample shows a weakly semiconducting property at high temperatures, it then reaches a maximum peak at intermediate temperatures around  $\sim 150$  K, and finally it follows a metallic behavior with lowering  $T$ . It is well known that CuO single chains in Pr123 and CuO double chains in Pr124 show semiconducting and metallic behaviors, respectively. The reduction heat treatment on the as-sintered sample in a vacuum results in the appearance of superconducting state with  $T_c = 22-27$  K, accompanied by the strongly metallic properties over a wide range of temperature (**Figure 6a**). For the present Pr247 sample with a reduction treatment for 72 h, a sharp superconducting transition appears at an onset temperature  $T_{c,on} = 26$  K and then it achieves a zero resistance state at  $T_{c,zero} = 22$  K.

Furthermore, to check bulk superconductivity, we performed to measure low-temperature dependence of magnetic susceptibility  $\chi$  of the 72-h-reduced superconducting sample measured at 5 mT under ZFC scan. **Figure 6b** exhibits diamagnetic signals below  $T_{c,on} = 26$  K for the 72-h-reduced sample. In addition, the superconducting volume fraction due to the shielding effect is estimated to be  $\sim 58\%$  from the ZFC values at 5 K. In the inset of **Figure 6**, the magnified data are plotted to clarify the definition of  $T_{c,on}$ . We note that the quenching procedure in

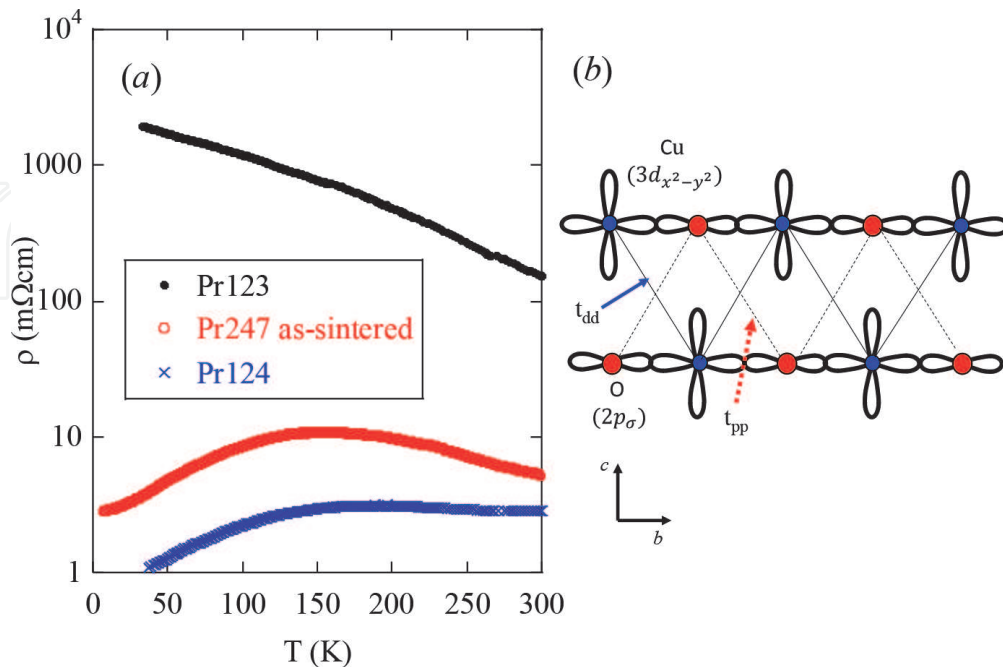


**Figure 5.**

(a) Temperature dependences of electric resistivities of the Pr123, Pr124, and as-sintered Pr247 compounds. (b) Schematic view of Cu( $3d_{x^2-y^2}$ ) orbitals and O( $2p_\sigma$ ) orbitals in a CuO double chain of  $\text{Pr}_2\text{Ba}_4\text{Cu}_7\text{O}_{15-\delta}$ . Here,  $t_{pp}$  and  $t_{dd}$  denote the hopping term between  $2p_\sigma$  orbitals at the nearest neighbor oxygen sites and that between  $3d_{x^2-y^2}$  orbitals at the nearest neighbor copper sites, respectively [32].

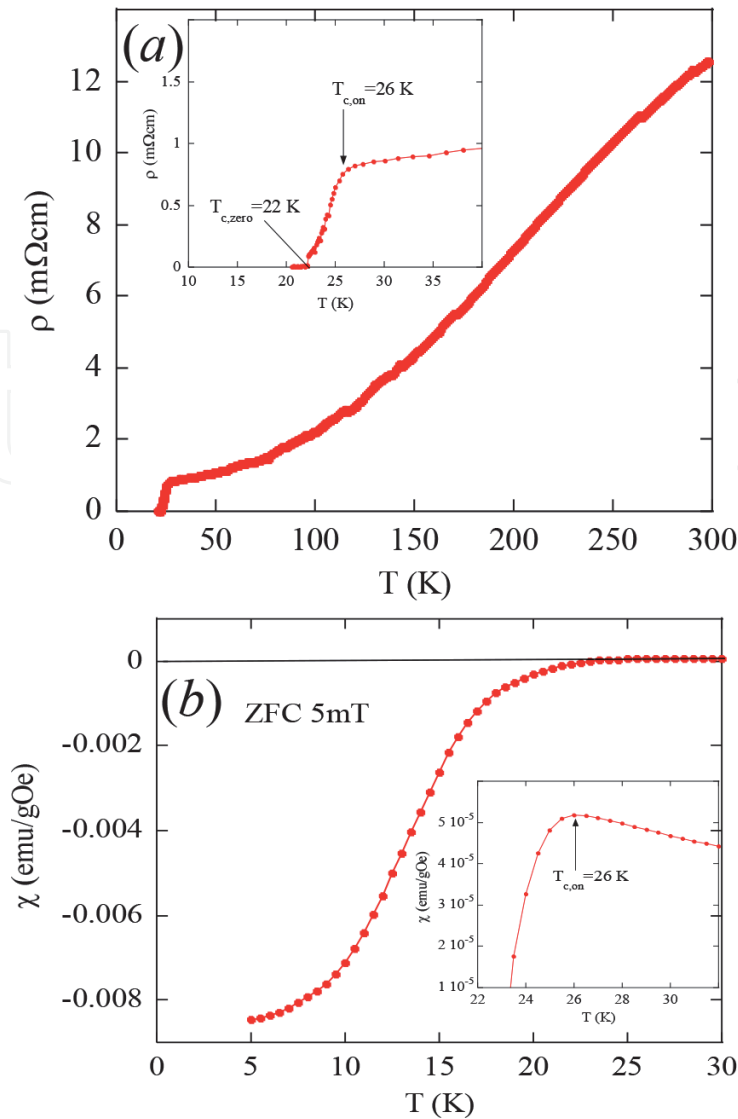


**Figure 6.**  
 (a) Temperature dependence of electric resistivity of the 72-h-reduced superconducting Pr<sub>247</sub> compound.  
 (b) Low-temperature dependence of magnetic susceptibility  $\chi$  of the 72-h-reduced superconducting sample measured at 5 mT under ZFC scan. In the insets, the magnified data are plotted to clarify the definition of  $T_{c,on}$ .

air promotes a sharp superconducting transition appearing at temperatures between  $T_{c,on}=26$  K and  $T_{c,zero}=22$  K.

### 3.1.2 Hall and pressure effects of Pr<sub>2</sub>Ba<sub>4</sub>Cu<sub>7</sub>O<sub>15- $\delta$</sub>

Furthermore, in **Figure 7**, we show the temperature dependences of the Hall coefficients  $R_H$  for the as-sintered non-superconducting and 48-h-reduced superconducting samples of Pr<sub>2</sub>Ba<sub>4</sub>Cu<sub>7</sub>O<sub>15- $\delta$</sub> . For comparison, the  $R_H$  values of the as-sintered sample are taken from our previous work [33], which are similar, in magnitude and temperature dependence, to  $R_H$  of Pr124 with a metallic CuO double-chain block. (**Figure 1a**) For the 48-h-reduced sample, the  $R_H$  data exhibit negative values in the limited temperature range between 30 and 100 K, accompanied by electron doping due to the reduced heat treatment in a vacuum. Moreover, we estimate  $R_H = -1.1 \times 10^{-3}$  cm<sup>3</sup>/C at 30 K, which is in good agreement with the published data [33].

In **Figure 7b**, we show the temperature dependences of electrical resistivities of the 48-h-reduced superconducting sample under hydrostatic pressures up to 2.0 GPa. The application of external pressure on the 48-h-reduced sample suppressed the superconductivity with increasing the applied pressure. In the case

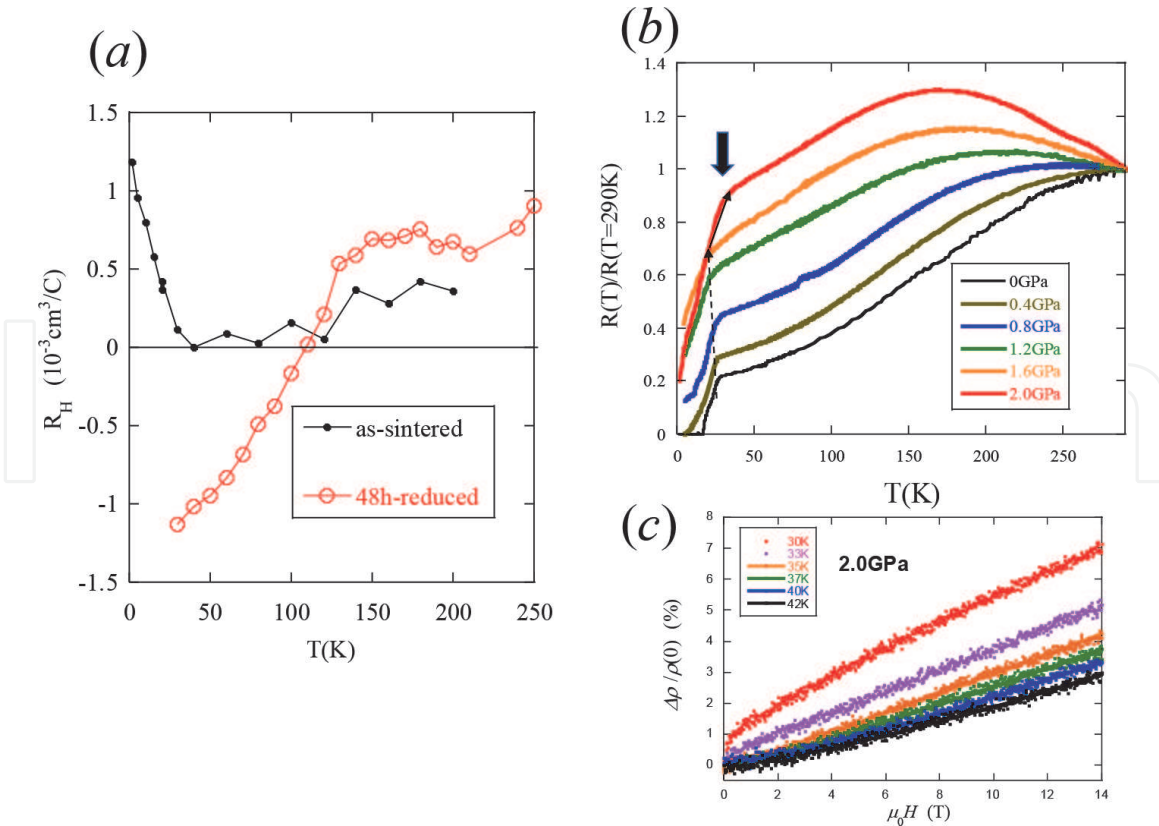


**Figure 7.**

(a) Temperature dependences of Hall coefficients for the as-sintered non-superconducting and 48-h-reduced superconducting Pr247 compounds. For comparison, the as-sintered data are cited from our previous paper [34]. (b) Temperature dependences of electrical resistivities of the 48-h-reduced superconducting Pr247 under various pressures up to 2.0 GPa. (c) Magneto-resistance effect (up to 14 T) of the 48-h-reduced superconducting Pr247 for temperatures close to 30 K under a maximum pressure of 2.0 GPa.

of applied pressures above 0.8 GPa, the zero-resistance state vanished and the high-temperature metallic properties were transferred to the semi-conducting behaviors, accompanied by a rapid increase in  $\rho$ . The onset temperature of superconducting transition  $T_{c,on}$  declined gradually from 26.5 K at ambient pressure through 24.1 K at 0.8 GPa down to 18.0 K at 1.6 GPa. However, the onset temperature was enhanced up to  $\sim 30$  K under a maximum pressure of 2.0 GPa.

The electronic phase diagram between normal and superconducting phases of a CuO double chain model has been clarified using the Tomonaga-Luttinger Liquid theory [32]. In the case of a shrinkage of the lattice spacing along  $c$ -axis between the two single chains of a CuO double-chain block, we expect the enhancement of both carrier hopping energies,  $t_{pp}$  and  $t_{dd}$ . Here, we define the hopping term between  $2p_\sigma$  orbitals at the nearest neighbor oxygen sites and that between  $3d_{x^2-y^2}$  orbitals at the nearest neighbor copper sites, as  $t_{pp}$  and  $t_{dd}$ , respectively (see **Figure 5b**). If we apply the external pressure on Pr247 including the CuO double chain block, it is theoretically predicted that the pressure induced enhancement of the hopping terms will result in a phase transition from the superconducting to normal phase. This theoretical prediction is qualitatively in agreement with the negative pressure effect on the superconducting phase observed in Pr247 [34].

We examined the magneto-resistance effect (up to 14 T) of the 48-h-reduced superconducting Pr247 for temperatures close to 30 K under a maximum pressure of 2.0 GPa, to establish a phase boundary between the superconducting and normal states. In **Figure 7c**, the MR data around 30 K tend to increase according to the upward convey behaviors at low fields. On the other hand, the MR around  $\sim 40$  K shows weak increases in the downward convey forms which is related to the model

of slightly warped Fermi surfaces. (in details, see [27]) This finding indicates that the applied magnetic field destroyed the superconducting isolated regions and enlarged further the normal-state majority phase, resulting in the observed MR phenomena near 30 K. The re-entrant superconducting behavior observed at 2.0 GPa is an open question to be resolved in future through the structure analysis under applied pressures [35].

## 3.2 Double perovskite photocatalytic semiconductor

### 3.2.1 Structural and valence-state properties of $Ba_2Tb(Bi,Sb)O_6$ samples

X-ray diffraction patterns of  $Ba_2TbBiO_6$  are shown in **Figure 8**. For the parent  $Ba_2TbBiO_6$  with a monoclinic structure (the space group  $I2/m$ ), the lattice parameters were estimated from the x-ray diffraction data to be  $a = 6.1099 \text{ \AA}$ ,  $b = 6.0822 \text{ \AA}$ ,  $c = 8.5939 \text{ \AA}$  and  $\beta = 89.888^\circ$ , which fairly agree with previous data [20]. The peak intensity of (101) reflection (the inset of **Figure 8**) is responsible for the degree of B-site ordering in the double-perovskite crystal structures. When the B site ordering is assumed to be  $\sim 70\%$ , the tiny profiles around the (101) peak are well fitted by the least squared method using the RIETAN-FP program [37].

For the  $Ba_2Pr(Bi,Sb)O_6$  system, the polycrystalline samples for  $x < 0.5$  are formed in almost single phases of the monoclinic structure, while the  $x \geq 0.5$  samples crystallize in a cubic structure with the space group  $Fm\bar{3}m$  [24]. Substitution of the smaller  $Sb^{5+}$  ( $0.60 \text{ \AA}$ ) ion at the  $Bi^{5+}$  ( $0.76 \text{ \AA}$ ) site causes a monotonic decrease in the lattice parameters. For  $Ba_2TbBi_{0.5}Sb_{0.5}O_6$ , we obtain the lattice parameters  $a = 8.4511 \text{ \AA}$  and  $\alpha = 90^\circ$ . **Figure 8b** shows tolerance factor vs. Sb content ( $x$ ) for  $Ba_2^{2+}Tb^{3+}Bi_{1-x}^{5+}Sb_x^{5+}O_6$  and  $Ba_2^{2+}Tb^{4+}M1_{1-x}^{4+}M2_x^{4+}O_6$  with  $M1^{4+} = Bi_{0.5}^{3+}Bi_{0.5}^{5+}$  and

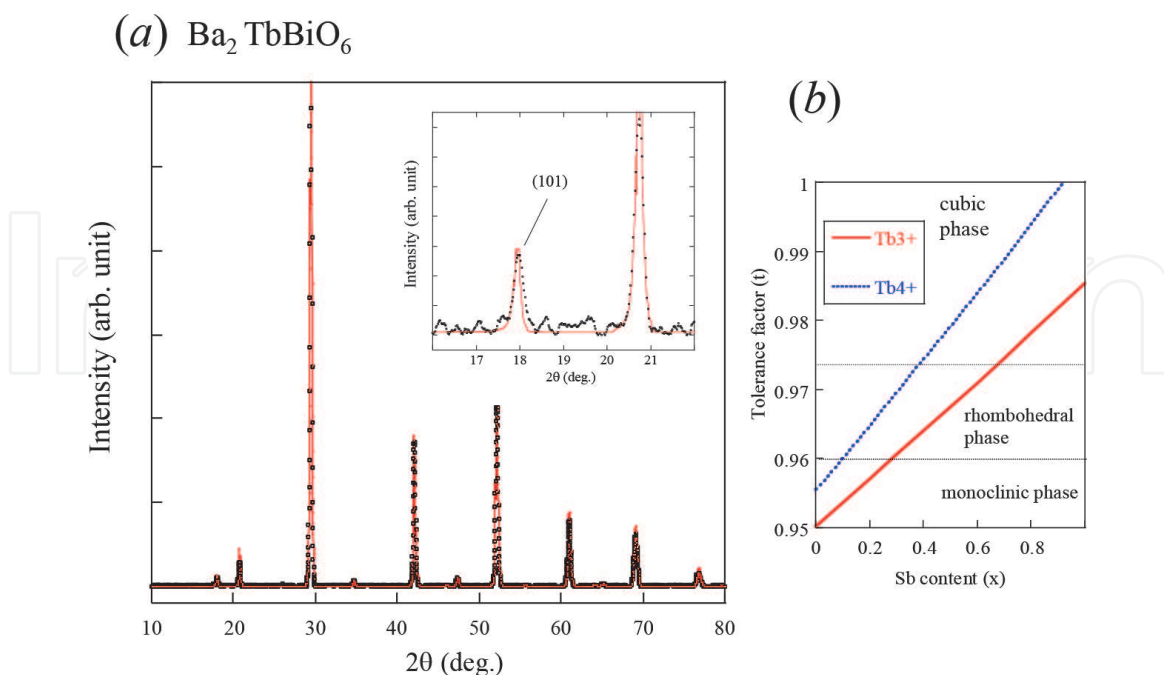


**Figure 8.** (a) X-ray diffraction patterns of  $Ba_2TbBiO_6$ . Inset shows the enlarged diffraction data. The emergence of (101) reflection indicates B-cation ordering which is characteristic of the ordered double-perovskite structure. (b) Tolerance factor vs Sb content for  $Ba_2TbBi_{1-x}Sb_xO_6$ . The solid and dotted lines denote  $Ba_2^{2+}Tb^{3+}Bi_{1-x}^{5+}Sb_x^{5+}O_6$  and  $Ba_2^{2+}Tb^{4+}M1_{1-x}^{4+}M2_x^{4+}O_6$  with  $M1^{4+} = Bi_{0.5}^{3+}Bi_{0.5}^{5+}$  and  $M2^{4+} = Sb_{0.5}^{3+}Sb_{0.5}^{5+}$ . The crystallographic phase diagram consisting of the monoclinic, rhombohedral and cubic phases is given as a function of tolerance factor in ref. [36].

$M2^{4+} = Sb_{0.5}^{3+}Sb_{0.5}^{5+}$ . The tolerance factor of double perovskite compounds  $Ba_2(Pr,Tb)(Bi,Sb)O_6$  is given by the following equation,

$$t = \frac{r_{Ba} + r_O}{\sqrt{2}\left(\frac{r_{Tb} + r_M}{2} + r_O\right)}, \quad (1)$$

where  $r_{Ba}$ ,  $r_O$ ,  $r_{Tb}$ , and  $r_{M=(Bi,Sb)}$  are the ionic radii of the respective ions (in details, refer to [24]). The crystallographic phase diagram consisting of the monoclinic, rhombohedral and cubic phases is given as a function of tolerance factor in ref. [36]. The crystal structures obtained for the  $x = 0$  and  $x = 0.5$  samples are almost consistent with the phase diagram reported. Assuming the tetravalent state of  $Tb^{4+}$ , we obtain the value of  $t = 0.97914$ , indicating the stability of a cubic structure for the  $x = 0.5$  sample. The microstructures and pelletized precursors for the  $Ba_2TbBiO_6$  parent sample prepared by the citrate pyrolysis method are shown in **Figure 2b** and **c**. The crystalline grains of the citrate sample have an average size ranging from about 0.2 to 0.5 micron. On the other hand, the grain diameters of the solid-state sample are distributed on a micron order scale and about one-order greater than those of the former. The citrate pyrolysis process fabricates uniformly dispersed grains with sub micron size compared with the solid-state preparation technique (see [24]).

The magnetic susceptibility data for the  $Ba_2Tb(Bi_{1-x},Sb_x)O_6$  compounds ( $x=0$  and 0.5) were measured as a function of temperature under a magnetic field of 0.1 T. (not shown here) The effective magnetic moments ( $\mu_{eff}$ ) are estimated from the magnetization data using the Curie–Weiss law. For the parent and  $x = 0.5$  citrate samples, we obtain  $\mu_{eff} = 8.91 \mu_B$  and  $8.86 \mu_B$ , as listed in **Table 2**. Moreover, we try to evaluate the ratio of the  $Tb^{3+}$  and  $Tb^{4+}$  ions using the equation,

$$\mu_{eff}^2 = y\mu_{eff}^2(Tb^{3+}) + (1 - y)\mu_{eff}^2(Tb^{4+}) \quad (2)$$

where  $\mu_{eff}(Tb^{3+}) = 9.72 \mu_B$  and  $\mu_{eff}(Tb^{4+}) = 7.94 \mu_B$ . For the parent and  $x = 0.5$  citrate samples, we obtain that the ratio of  $Tb^{3+}$  and  $Tb^{4+}$  ions is 0.52 : 0.48 and 0.49 : 0.51, respectively. The mixed valence state expected from the magnetic data qualitatively consists with the above discussion on the stability of cubic structure for the  $x = 0.5$  sample. The magnetic data suggest that about half of Re ions (Re = Pr and Tb)

Sample no.	Composition	Synthetic method	Crystal symmetry	$\mu_{eff} (\mu_B)$	Experimental data
#T1	$Ba_2TbBiO_6$	citrate pyrolysis	monoclinic	8.91	IPA, MB, Opt.
#T2	$Ba_2TbMO_6$ M = $Bi_{0.5}Sb_{0.5}$	citrate pyrolysis	cubic	8.86	IPA, MB, Opt.
#T3	$Ba_2TbBiO_6$	solid state	monoclinic	9.07	IPA, MB, Opt.
#P1	$Ba_2PrBiO_6$	citrate pyrolysis	monoclinic <sup>a</sup>	3.08 <sup>a</sup>	MB
#P2	$Ba_2PrSbO_6$	citrate pyrolysis	cubic <sup>a</sup>	3.0 <sup>a</sup>	MB
#P3	$Ba_2PrBiO_6$	solid state	monoclinic <sup>b</sup>	3.15 <sup>b</sup>	MB

The effective magnetic moments  $\mu_{eff}$  were estimated from the magnetization data using the Curie–Weiss law. IPA, MB and Opt. denote gaseous 2-propanol decomposition, methylene blue degradation, and optical measurements, respectively.

<sup>a</sup>Ref. [24].

<sup>b</sup>Ref. [38].

**Table 2.** Sample details of  $Ba_2(Pr,Tb)(Bi,Sb)O_6$  used in the experiments.

are oxidized to the tetravalent state over the whole range of Sb substitution [24]. In a previous analysis of X-ray photoemission spectroscopy [39], it has been shown that a predominant peak of  $\text{Pr}^{3+}$  coexists with a smaller shoulder structure of  $\text{Pr}^{4+}$ , giving further evidence for the mixed valence state of the Pr ion.

### 3.2.2 Photocatalytic and optical properties of $\text{Ba}_2\text{Tb}(\text{Bi},\text{Sb})\text{O}_6$ samples

Next, the visible-light induced decomposition experiment using IPA gas was carried out, to examine photocatalytic activities of the powder samples.

In **Figure 4a**, the temporal variation of evolved  $\text{CO}_2$  concentration after visible light irradiation are shown for the  $\text{Ba}_2\text{TbBiO}_6$  citrate and solid state samples. For comparison, the data for the Sb50% substituted  $\text{Ba}_2\text{Tb}(\text{Bi}_{0.5},\text{Sb}_{0.5})\text{O}_6$  sample are also given. The  $\text{CO}_2$  concentrations for both the citrate and solid state  $x = 0$  samples rapidly rise at the initial 20 min and then show a gradual increase at further illumination time. For the Sb50% substituted sample, no clear evolution of  $\text{CO}_2$  was detected. It is expected that the heavy substitution of Sb ion at the B-site causes the band gap opening and considerably reduces the formation of electron-hole pairs, resulting in a strong suppression of the photocatalytic reaction processes. In our previous study [38], we investigated the influence of the band gap opening due to the Sb substitution on the basis of first-principles electric structure calculation. The Sb substitution at Bi site removes the Bi-orbitals and makes the corresponding band gap enlarged. The photocatalytic activity exhibits strong dependence of the Sb substitution, which is associated with the enhancement of the band gap energy. It is true that the photocatalytic behavior for the solid state sample is similar to that of the citrate sample. However, the evolved  $\text{CO}_2$  quantities of the  $x=0$  citrate sample are about twice as large as the data of the corresponding solid state sample, as shown in **Figure 4a**. The improved photocatalytic activity of the  $\text{Ba}_2\text{TbBiO}_6$  citrate sample is attributed to its morphology, where fine polycrystalline grains with a sub micron order are homogeneously dispersed.

Furthermore, we demonstrated photocatalytic degradation of methylene blue (MB) vs. visible light irradiation time for the end-member samples with  $\text{Ba}_2(\text{Pr},\text{Tb})\text{BiO}_6$  and  $\text{Ba}_2\text{PrSbO}_6$  compositions. For comparison, the MB data of the  $\text{Ba}_2\text{PrSbO}_6$  solid-state sample are given. Here, the MB degradation rate (%) is given by  $(C(0) - C(t))/C(0) \times 100$ , where the peak intensities located around  $\lambda = 665$  nm at the initial and final concentrations at different time intervals are defined as  $C(0)$  and  $C(t)$ , respectively. **Figure 9a** shows the MB degradation rate after the visible light irradiation for  $\text{Ba}_2\text{PrBiO}_6$  and  $\text{Ba}_2\text{PrSbO}_6$  samples. In **Figure 9b** and **c**, the typical absorbance spectra and corresponding MB solutions for  $\text{Ba}_2\text{PrSbO}_6$  at different irradiation time intervals are also displayed. The MB degradation rates under visible light irradiation show rapid increases due to Sb-substitution. For the Sb50% substituted  $\text{Ba}_2\text{Tb}(\text{Bi}_{0.5},\text{Sb}_{0.5})\text{O}_6$  sample, the highest performance of MB degradation was observed. The citrate parent sample of  $\text{Ba}_2\text{PrSbO}_6$  exhibits higher degradation in comparison with the data of the solid-state sample with the identical composition. For  $\text{Ba}_2\text{PrBiO}_6$ , the effect of Sb-substitution on the photocatalytic degradation of MB is in direct contrast to that on the IPA decomposition under visible light irradiation.

Finally, we carried out the optical measurements on the  $\text{Ba}_2\text{Tb}(\text{Bi}_{1-x},\text{Sb}_x)\text{O}_6$  ( $x=0$  and  $0.5$ ) powder samples by the diffuse reflectance method. In the first step, we transformed the observed reflectance data to the absorption coefficient  $\alpha_{\text{KM}}$  by applying the conventional Kubelka-Munk function. In the next step, extrapolating the tangent line to the  $\varepsilon_p$  axis near the band edge, we evaluate the energy band gap from the intersection following the equation

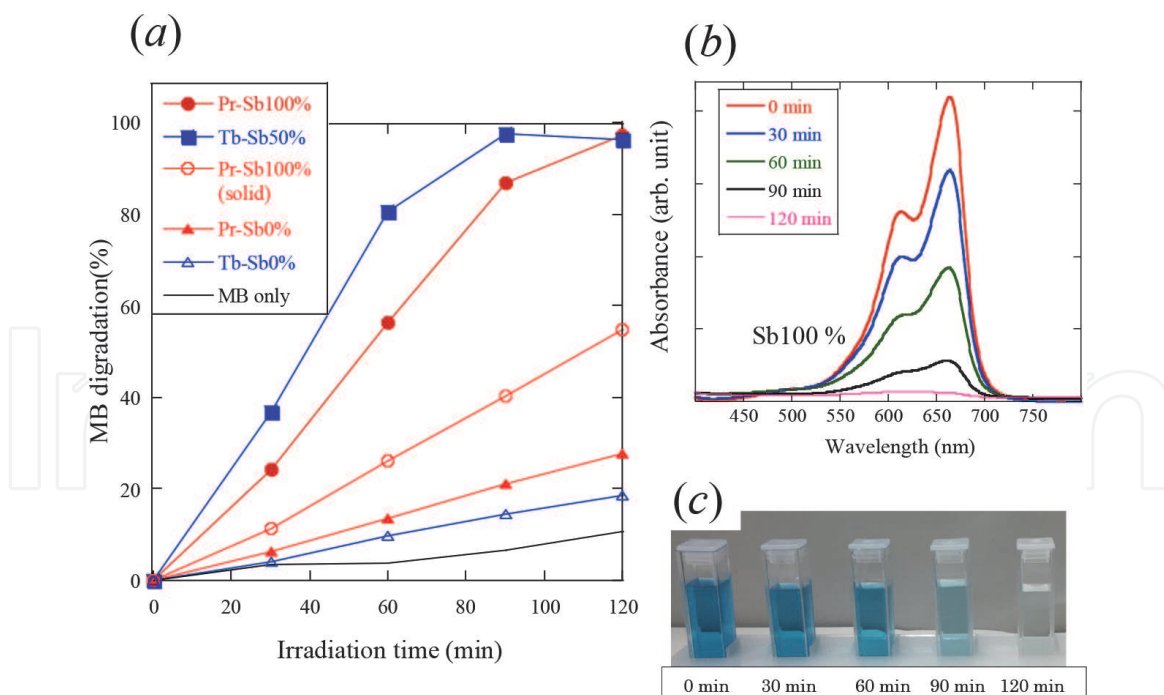


**Figure 9.**

(a) Photocatalytic degradation of methylene blue (MB) vs visible light irradiation time for  $Ba_2(Pr,Tb)(Bi,Sb)O_6$  citrate pyrolysis samples. For comparison, the MB data of the  $Ba_2PrSbO_6$  solid-state sample are given. (b) Absorbance spectra as a function of visible light irradiation time for the MB degradation in the case of  $Ba_2PrSbO_6$  citrate pyrolysis sample. (c) Photocatalytic variations of the MB solutions at different irradiation time intervals.

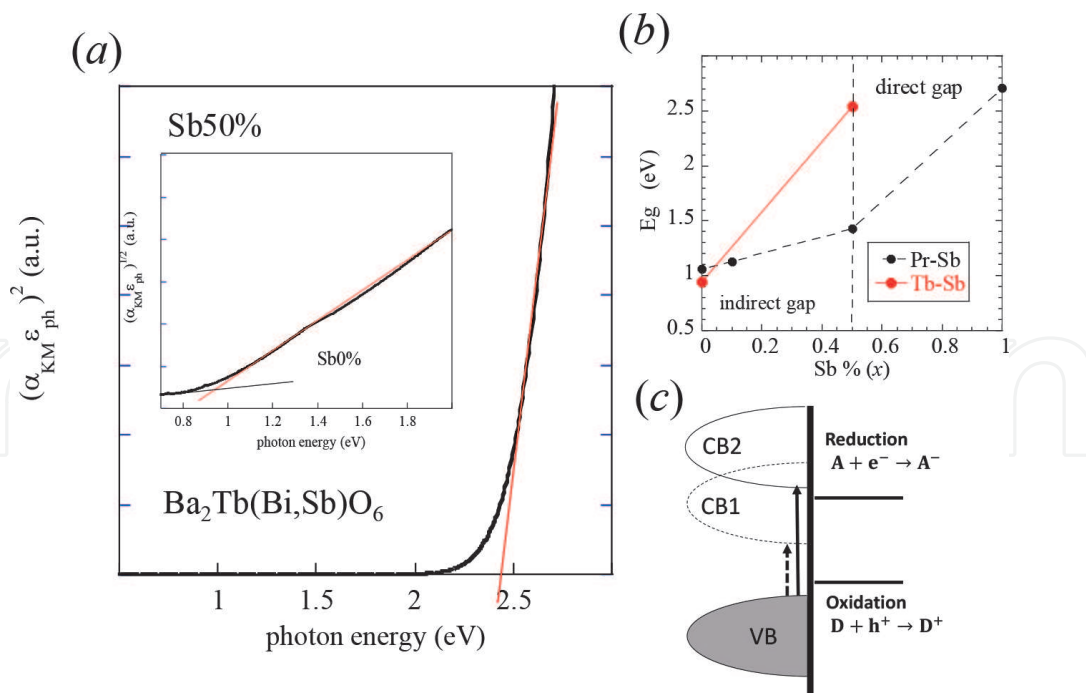


**Figure 10.**

(a) Optical properties of  $Ba_2Tb(Bi_{1-x},Sb_x)O_6$  ( $x=0$  and  $0.5$ ).  $(\alpha_{KM}\epsilon_p)^2$  vs  $\epsilon_p$  for the  $x = 0.5$  sample are plotted as a function of  $\epsilon_p$ . The inset shows plots of  $(\alpha_{KM}\epsilon_p)^{1/2}$  vs  $\epsilon_p$ . For the  $x = 0$  sample,  $E_g$  is estimated from an intersection point of base line and straight line by extrapolation. (b) Band gap energies vs Sb content ( $x$ ) for  $Ba_2Tb(Bi_{1-x},Sb_x)O_6$  ( $x=0$  and  $0.5$ ). The data of  $Ba_2Pr(Bi,Sb)O_6$  are cited from our previous work [24]. (c) Schematic illustration between the semiconductor band positions and the surface redox reactions in photocatalysis. The valence band (VB) is located to facilitate oxidation, but the lower conduction band (CB1) is not sufficiently positioned to facilitate reduction. The higher conduction band (CB2) is suitable for promoting effective reduction process.

$$(\alpha\varepsilon_p)^n \propto (\varepsilon_p - E_g), \quad (3)$$

where  $\alpha$ ,  $\varepsilon_p$ , and  $E_g$  are the absorption coefficient, the photon energy, and the band gap energy. The exponents,  $n = 2$  and  $n = 1/2$ , are responsible for direct and indirect optical transitions, respectively [18, 19]. In **Figure 10a**, the absorption coefficient,  $(\alpha_{\text{KM}}\varepsilon_p)^2$  is plotted as a function of  $\varepsilon_p$  for the  $x=0.5$  sample. In the inset of **Figure 10a**,  $(\alpha_{\text{KM}}\varepsilon_p)^{1/2}$  vs.  $\varepsilon_p$  are shown for the  $x=0$  sample. We obtain that  $E_g = 0.92$  eV at  $x=0$  and 2.45 eV at  $x=0.5$ , assuming indirect and direct photon transitions, respectively. The magnitude of the energy band gap is enhanced due to the Sb substitution.

In **Figure 10c**, schematic view between the semiconductor band positions and the the surface redox reactions in photocatalysis is presented. The valence band (VB) is located to facilitate oxidation, but the lower conduction band (CB1) is not sufficiently positioned to facilitate reduction. The higher conduction band (CB2) is needed to promote reduction process. Applying the present band model to the photocatalytic activities observed for  $\text{Ba}_2\text{Tb}(\text{Bi},\text{Sb})\text{O}_6$ , the parent compounds with smaller energy band gap of nearly 1 eV are responsible for the lower energy level of conduction band (CB1) edge. On the other hand, from the effect of band gap opening due to Sb substitution, we believe that the CB2 band model is valid in the heavily Sb substituted samples. The former is closely related to facilitate oxidation reactions at the surface for the IPA decomposition process. In the latter compounds with the larger energy band gaps of  $\sim 2.5$  eV, the MB degradation is strongly promoted in contrast to that of the former compounds. These findings indicate that the conduction band edge of the heavily Sb substituted samples is optimized.

#### 4. Conclusions

A citrate pyrolysis technique is a unique route to prepare reactive precursor mixtures through an ignition process of concentrated aqueous solution including metallic ions of stoichiometric composition. This procedure enables to synthesize highly homogeneous and fine powders for functional materials. The double-chain based superconductor  $\text{Pr}_2\text{Ba}_4\text{Cu}_7\text{O}_{15-\delta}$  and double perovskite photocatalytic semiconductor  $\text{Ba}_2\text{Tb}(\text{Bi},\text{Sb})\text{O}_6$  were synthesized by using the citrate pyrolysis technique.

The TEM image of the 48-h-reduced Pr247 revealed that CuO single-chain and double-chain blocks are alternately stacked along the  $c$ -axis such as  $\{-D-S-D-S-\}$  sequence. For the present Pr247 sample with a reduction treatment for 72 h, a sharp superconducting transition appeared at an onset temperature  $T_{\text{c,on}}=26$  K accompanied by a zero-resistance state at  $T_{\text{c,zero}}=22$  K. The superconducting volume fraction estimated from the magnetization measurement reached an excellent value of  $\sim 58\%$ . Both reduction treatment in a vacuum and subsequent quenching procedure are needed to realize higher superconductivity due to further oxygen defects. For the 48-h-reduced sample, the  $R_H$  data exhibited negative values in the limited temperature range between 30 and 100 K, accompanied by electron doping due to the reduced heat treatment in a vacuum. The re-entrant superconducting behavior observed at 2.0 GPa is an open question to be resolved in future through detailed structure analysis under applied pressures.

The polycrystalline samples for  $\text{Ba}_2\text{Tb}(\text{Bi}_{1-x},\text{Sb}_x)\text{O}_6$  ( $x = 0$  and 0.5) were formed in the monoclinic and cubic crystal structures. The magnetic data suggest that about half of Tb ions are oxidized to the tetravalent state over the wide range of Sb substitution, which is a common trend in the case of  $\text{Ba}_2\text{Pr}(\text{Bi},\text{Sb})\text{O}_6$ . For  $\text{Ba}_2\text{Tb}$

(Bi<sub>1-x</sub>Sb<sub>x</sub>)O<sub>6</sub>, we estimated  $E_g = 0.92$  eV at  $x=0$  and 2.45 eV at  $x=0.5$ , assuming indirect and direct photon transitions, respectively.

We conducted the gaseous 2-propanol (IPA) and methylene blue (MB) degradation experiments under a visible light irradiation, to evaluate photocatalytic activities of the powder samples. The band gap opening due to the heavy Sb substitution suppresses the formation of electron-hole pairs, causing a decrease of the photocatalytic reaction processes in the IPA decomposition. The MB degradation rates under visible light irradiation show rapid increases due to Sb-substitution. For the Sb50% substituted Ba<sub>2</sub>Tb(Bi<sub>0.5</sub>Sb<sub>0.5</sub>)O<sub>6</sub> sample, the highest performance of MB degradation was observed. In the Ba<sub>2</sub>(Pr,Tb)(Bi,Sb)O<sub>6</sub> system, the effect of Sb-substitution on the photocatalytic degradation of MB is in direct contrast to that on the IPA decomposition under visible light irradiation. We conclude that the citrate pyrolysis samples of Ba<sub>2</sub>Tb(Bi,Sb)O<sub>6</sub> exhibit excellent performances in comparison with the data of the solid-state samples with the identical composition. The enhanced photocatalytic properties in the citrate samples are attributed to their morphology, where fine particles are homogeneously distributed with a sub micron order.

## Acknowledgements

This work was supported in part by MEXT Grands-in-Aid for Scientific Research (JPSJ KAKENHI Grants No. JP19K04995). We thank A. Sato, T. Teramura, and Y. Nakarokkaku for their supports in experiments.

## Author details

Tatsuya Senzaki<sup>1</sup>, Michiaki Matsukawa<sup>1\*</sup>, Takanori Yonai<sup>1</sup>, Haruka Taniguchi<sup>1</sup>, Akiyuki Matsushita<sup>2</sup>, Takahiko Sasaki<sup>3</sup> and Mokoto Hagiwara<sup>4</sup>

<sup>1</sup> Faculty of Science and Engineering, Iwate University, Morioka, Japan

<sup>2</sup> National Institute for Materials Science, Tsukuba, Japan

<sup>3</sup> Institute for Materials Research, Tohoku University, Sendai, Japan

<sup>4</sup> Kyoto Institute of Technology, Kyoto, Japan

\*Address all correspondence to: matsukawa@iwate-u.ac.jp

## IntechOpen

© 2021 The Author(s). Licensee IntechOpen. This chapter is distributed under the terms of the Creative Commons Attribution License (<http://creativecommons.org/licenses/by/3.0>), which permits unrestricted use, distribution, and reproduction in any medium, provided the original work is properly cited. 

## References

- [1] L. A. Chick, L. R. Pederson, G. D. Maupin, J. L. Bates, L. E. Thomas, G. J. Exarhos, *Materials Letters*, vol. 10, 6-12, 1990.
- [2] K. Koyama, A. Junod, T. Graf, G. Triscone, and J. Muller, *Physica C*, vol.185-189, 66-70, 1991.
- [3] M. Hagiwara, T. Shima, T. Sugano, K. Koyama, and M. Matsuura, *Physica C*, vol. 445-448, 111-114, 2006.
- [4] M. Uehara, T. Nagata, J. Akimitsu, H. Takahashi, N. Mori, and K. Kinoshita, *J. Phys. Soc. Jpn.* 65 (1996) 2764.
- [5] M. Matsukawa, Y. Yamada, M. Chiba, H. Ogasawara, T. Shibata, A. Matsushita, and Y. Takano, *Physica C* 411 (2004) 101.
- [6] S. Watanabe, Y. Yamada and S. Sasaki, *Physica C* 426-431 (2005) 473.
- [7] L. Soderholm, K. Zhang, D. G. Hinks, M. A. Beno, J. D. Jorgensen, C. U. Segre, I. K. Schuller, *Nature* 328 (1987) 604.
- [8] S. Horii, Y. Yamada, H. Ikuta, N. Yamada, Y. Kodama, S. Katano, Y. Funahashi, S. Morii, A. Matsushita, T. Matsumoto, I. Hirabayashi, and U. Mizutani, *Physica C* 302 (1998) 10.
- [9] T. Mizokawa, C. Kim, Z. -X. Shen, A. Ino, T. Yoshida, A. Fujimori, M. Goto, H. Eisaki, S. Uchida, M. Tagami, K. Yoshida, A. I. Rykov, Y. Siohara, K. Tomimoto, S. Tajima, Yuh Yamada, S. Horii, N. Yamada, Yasuji Yamada, and I. Hirabayashi, *Phys. Rev. Lett.* 85 (2000) 4779.
- [10] P. Bordet, C. Chaillout, J. Chenavas, J. L. Hodeau, M. Marezio, J. Karpinski, and E. Kaldis, *Nature* 334 (1988) 596.
- [11] Y. Yamada, S. Horii, N. Yamada, Z. Guo, Y. Kodama, K. Kawamoto, U. Mizutani, and I. Hirabayashi, *Physica C* 231(1994)131.
- [12] T. Konno, M. Matsukawa, H. Taniguchi, J. Echigoya, A. Matsushita, M. Hagiwara, T. Miyazaki, K. Sano, Y. Ono, Y. Yamada, T. Sasaki, and Y. Hayasaka, *Physica C* 521-522 (2016) 13.
- [13] S. Vasala, and M. Karppinen, *Prog. Solid State Chem.*, vol. 43, pp. 1-31, 2015.
- [14] K. -I. Kobayashi, T. Kimura, H. Sawada, K. Terakura, and Y. Tokura, *Nature*, vol. 395, pp. 677, 1998.
- [15] R. Ramesh, and N. A. Spaldin, *Nature Materials*, vol. 2, pp. 21, 2007.
- [16] A. Fujishima, and K. Honda, *Nature*, vol. 238, pp. 37, 1972.
- [17] H. W. Eng, P. W. Barnes, B. M. Auerand, and P. M. Woodward, *J. Solid State Chem.*, vol.175, pp. 94, 2003.
- [18] T. Hatakeyama, S. Takeda, F. Ishikawa, A. Ohmura, A. Nakayama, Y. Yamada, A. Matsushita, and J. Yea, *J. Cer. Soc. Jpn.*, vol. 118, pp.91-95, 2010.
- [19] A. Matsushita, T. Nakane, T. Naka, H. Isago, Y. Yamada, and Yuh Yamada, *Jpn. J. Appl. Phys.*, vol. 51, pp. 121802-1-5, 2012.
- [20] William T. A. Harrison, K. P. Reis, A. J. Jacobson, L. F. Schneemeyer, and J. V. Waszczak, *Chem. Mater.*, vol. 7, pp. 2161-2167, 1995.
- [21] X. Chen, S. Shen, L. Guo, and S. Mao, *Chem. Rev.* vol.110, 6503-6570, 2010.
- [22] D. Sudha, and P. Sivakumar, *Chemical Engineering and Processing*, vol. 97, 112-133, 2015.
- [23] B. Ohtani, *Catalysts*, vol.3, 942-953, 2013.
- [24] A. Sato, M. Matsukawa, H. Taniguchi, S. Tsuji, K. Nishidate, S.

- Aisawa, A. Matsushita, and K. Zhang, *Solid State Science*, 107, 10635, 2020.
- [25] A. Housa, H. Lachheb, M. Ksibi, E. Elaloui, C. Guillard, J.M. Herrmann, *Applied Catalysis B31*, 145, 2001.
- [26] K. Honnami, M. Matsukawa, T. Senzaki, H. Taniguchi, K. Takahashi, T. Sasaki, M. Hagiwara, *Physica C585* (2021) 1353869.
- [27] M. Kuwabara, M. Matsukawa, K. Sugawara, H. Taniguchi, A. Matsushita, M. Hagiwara, K. Sano, Y. Ono, and T. Sasaki, *J. Phys. Soc. Jpn.* 85 (2016) 124704.
- [28] J. W. Tang, Z. G. Zou, and J. H. Ye, *J. Phys. Chem. C*, vol. 111, pp. 12779-12785, 2007.
- [29] T. Murase, H. Irie, and K. Hashimoto, *J. Phys. Chem. B*, vol. 108, 15803-15807 (2004)
- [30] Y. Yamada and A. Matsushita, *Physica C* 426-431 (2005) 213.
- [31] M. Hagiwara, S. Tanaka, T. Shima, K. Gotoh, S. Kanda, T. Saito, and K. Koyama, *Physica C* 468 (2008) 1217.
- [32] K. Sano, Y. Ono, and Y. Yamada, *J. Phys. Soc. Jpn.*, 74 (2005) 2885.
- [33] J. Tada, M. Matsukawa, T. Konno, S. Kobayashi, M. Hagiwara, T. Miyazaki, K. Sano, Y. Ono, and A. Matsushita, *J. Phys. Soc. Jpn.* 82 (2013) 105003.
- [34] F. Ishikawa, K. Fukuda, S. Sekiya, A. Kaeriyama, Y. Yamada and A. Matsushita, *J. Phys. Soc. Jpn.*, 76 (2007) Suppl. A 92.
- [35] H. Taniguchi, A. Nakayama, M. Matsukawa, S. Nakano, M. Hagiwara and T. Sasaki, *J. Phys. Soc. Jpn.* 90 (2021) 015001.
- [36] S. Otsuka, and Y. Hinatsu, *J. Solid State Chem.*, vol. 227, pp. 132-141, 2015.
- [37] F. Izumi and K. Momma, *Solid State Phenom.* 130 (2007) 15.
- [38] H. Taniguchi, M. Matsukawa, K. Onodera, K. Nishidate, and A. Matsushita, *IEEE Transactions on Magnetics*, 55(2), (2019) 2400404.
- [39] K. Onodera, T. Kogawa, M. Matsukawa, H. Taniguchi, K. Nishidate, A. Matsushita, and M. Shimoda, *J. Phys. Conf. Ser.*, vol. 969, pp. 012122-1-6, 2018.